Scaling Microseismic Cloud Shape during Hydraulic Stimulation using Permeability and *In-situ* Stress

Y. Mukuhira[1], M. Yang[1,2], T. Ishibashi[3], K. Okamoto[3], H. Moriya[4], Y. Kumano[5], H. Asanuma[4], S. A. Shapiro[6], J. Rubinstein[7], T. Ito[1], K. Yan[1,2], Y. Zuo[2]

[1]Institute of Fluid Science, Tohoku University. [2]State Key Laboratory of Oil and Gas Geology and Exploitation, Chengdu University of Technology. [3]Fukushima Renewable Energy Institute, National Institute of Advanced Industrial Science and Technology. [4]School of Engineering, Tohoku University. [5]JAPEX Co., Ltd. [6]Freie Universität Berlin. [7]United States Geological Survey.

Corresponding author: Yusuke Mukuhira (mukuhira@tohoku.ac.jp)

Key Points:

- Microseismic cloud shape is correlated to the permeability tensor and *in-situ* stress ratio.
- Microseismic cloud growth is mainly controlled by *in-situ* stress if there is sufficient variation in existing fracture orientation
- Microseismic cloud shape can be forecasted macroscopically with the *in-situ* stress ratio, for use in designing an energy extraction system

Abstract

Forecasting microseismic cloud shape as a proxy of stimulated rock volume is essential for the design of an energy extraction system. The microseismic cloud created during hydraulic stimulation is known empirically to extend in the maximum principal stress direction. However, this empirical relationship is often inconsistent with reported results, and the cloud growth process remains poorly understood. This study investigates microseismic cloud growth using data obtained from a hydraulic stimulation project in Basel, Switzerland, and explores its correlation with measured *in-situ* stress. We applied principal component analysis to a time series of microseismic distribution for macroscopic characterization of microseismic cloud growth in two- and three-dimensional space. The microseismic cloud in addition to extending in the direction of maximum principal stress expanded to the direction of intermediate principal stress too. The orientation of the least microseismic cloud growth was stable and almost identical to the minimum principal stress direction. Following the stimulation, the orientation of microseismic cloud growth was consistent with the *in-situ* stress direction. Further, microseismic cloud shape ratios showed good agreement when compared with *in-situ* stress magnitude. The permeability tensor estimated from microseismicity also presented good correlation in terms of direction and magnitude with microseismic cloud growth. We show that *in-situ* stress plays a dominant role by controlling the permeability of each existing fracture in the reservoir fracture system. Consequently, microseismic cloud growth can be scaled by *in-situ* stress if there is sufficient variation in the existing faults.

Plain Language Summary

In the next generation of geothermal development, a massive volume of fluid is injected into the subsurface to create a potential geothermal reservoir or stimulate the formation's conductivity. In that process, water migration can be tracked by small earthquakes that are rarely felt by humans. The region of small earthquakes can be regarded as an active geothermal reservoir. The reservoir's shape is important for the assessment and design of the energy extraction system. However, it is difficult to forecast the shape of a possible geothermal reservoir prior to fluid injection. This study investigated the time series change in the shape of the region of small earthquakes caused by fluid injection using the data from the geothermal project at Basel, Switzerland. We found that the region's shape is correlated to the local stress when the reservoir hosted various existing fractures. Thus, the geothermal reservoir shape can be forecasted with regional stress in advance, for better assessment of geothermal development.

1 Introduction

A stable energy supply is critically important to sustainably maintain broad economic and social activities. Additionally, the transition from hydrocarbon resources associated with carbon dioxide (CO_2) emissions to renewable energy is necessary to mitigate global warming and its various associated risks. Geothermal energy is one of the most promising renewable energy sources, as its stability is suitable for baseload. Several attempts have been made to increase geothermal energy use even in non-volcanic regions (Evans et al., 2012) through the development of an enhanced geothermal system (EGS). In EGS development, geothermal energy is extracted from a deeper depth than that would be utilized in volcanic regions in order to access high-temperature geothermal resources and generate energy more economically. Based on permeability and the condition of fluid richness in the target formation, an engineering operation is typically employed to either increase the permeability or to feed in fluid as a heat exchange medium; that is, fluid injection. In many cases of EGS, such fluid injection is a means of hydraulic stimulation to improve the permeability through hydro-shearing of existing fractures. Naturally, a geothermal reservoir, which often consists of granite, hosts several existing fractures; thus, boreholes often meet these existing fractures. In this case, fluid is injected at a lower wellhead pressure than the minimum principal stress (σ_3). The injected water migrates via the existing fracture system in the reservoir, and increased pore pressure concurrently destabilizes the existing faults. When friction decreases to a sufficient amount to yield shear stress, shear slip occurs on the existing fractures (Pine & Batchelor, 1984; Zoback, 2007), resulting in microseismicity. The magnitude of such microseismicity is typically smaller than 2, but in some cases earthquakes larger than magnitude 2 have occurred (Ellsworth, 2013; Evans et al., 2012; Majer et al., 2007). This is the main process of EGS engineering operations, as shear slip on existing fractures enhances the reservoir permeability (e.g., Watanabe et al., 2008; Yeo et al., 1998).

Measurement and analysis of microseismicity are essential parts of EGS, involving the monitoring of hydraulic stimulation and visualization of the shape and geometry of the artificial reservoirs. Microseismic data are automatically processed, and the hypocenter and magnitude of microseismicity is determined (e.g., Dyer et al., 2008; Gharti et al., 2010; Grigoli et al., 2016). Due to uncertainty in the phase arrival and velocity model, microseismic hypocenters often show a cloud shape, i.e., the microseismic cloud (hereafter, the MS cloud), regardless of the magnitude. Post analysis by experts includes refined phase picking, relocation of the hypocenter, estimation of the source parameters such as moment magnitude and stress drop, and determination of the focal mechanisms. Relocated hypocenters often delineate a much sharper existing fracture system than the automatically determined MS cloud. Therefore, well-determined MS cloud information can be used as a proxy for stimulated rock volume and can be used to indicate the location of production wells, as well as to identify the fracture system for heat exchange and aid in reservoir management (e.g., Dyer et al., 2008; Evans, 2005; Majer et al., 2007).

Many have shown that the MS cloud typically grows in the direction of maximum principal stress (σ_1) (e.g., Roff, W. S. Phillips, 1996; Häring et al., 2008; Tezuka & Niitsuma, 2000). The conceptual fracture model for earthquake swarms in volcanic regions (Hill, 1977) and a similar model proposed by Sibson (1996) have often been used to interpret MS cloud growth (Evans et al., 2005; Häring et al., 2008). In these models, the conjugate fractures (which can be regarded as optimally oriented faults) and extensional fractures comprise the fracture mesh. The firsts faults that slip following fluid injection, are typically optimally oriented with respect to the *in-situ* stress field. These faults strike approximately 30° off the direction of σ_1. Microseismic events often occur on both optimally oriented conjugate faults, if they both exist. Consequently, the MS cloud grows in the direction of σ_1 from a macroscopic perspective, as presented in Häring et al. (2008). Meanwhile, the faults parallel to σ_1 can also have shear slip after pore pressure increases sufficiently. These faults are subjected to σ_3 such that they have the highest permeability according to the theory between permeability and effective normal stress (e.g., Miller, 2015; Rice, 1993; Willis-Richards et al., 1996). Such a fault would accommodate significant fluid flow once injected fluid reached it, regardless of an occurrence of shear slip. Non-optimally oriented faults (especially conjugate forms) also contribute to the extension of the

MS cloud in the direction of σ_1 with the increase of pore pressure, although they also contribute to expanding the width of the MS cloud due to their components that are perpendicular to the σ_1 direction. Thus, the MS cloud should extend in the direction of σ_1 if there are existing fracture distributions consistent with *in-situ* stress.

This is similar to the well-known insight of fracture propagation at the time of hydraulic fracturing. Fracture initiation occurs when fluid pressure exceeds σ_3 and tensile strength. Nucleated fractures extend in the direction of σ_1 (Hubbert & Willis, 1972); thus, the hypocenter distribution of microseismicity observed in the case of hydraulic fracturing also extends in the orientation of σ_1. The MS cloud deviates from the orientation of σ_1 once the extending fractures meet the natural fracture systems, or it thickens if branching occurs. Thus, MS cloud growth in the case of hydraulic fracturing is attributed to much simpler flow and failure phenomena than it would be in the case of hydraulic stimulation into fracture networks.

In the EGS projects of Basel, Switzerland, and Soultz, France, both of which are located within the Rhine graben, the shape of the MS cloud was consistent with the σ_1 orientation (Evans et al., 2005; Häring et al., 2008; Mukuhira et al., 2013; Soma et al., 2007). However, this empirical relationship cannot always explain the shape of observed MS clouds. As a counter-example, the hot fracture rock project in the Cooper Basin, Australia, had a different feature, in that the observed MS cloud was mainly delineated by one or a few subhorizontal fractures (Baisch et al., 2006); the planar MS cloud did not grow to the σ_1 orientation. Thus, the MS cloud of the Cooper Basin was heavily controlled by the dominant horizontal existing fractures as opposed to *in-situ* stress. Another counter-example is the case of the Fenton Hill Hot Dry Rock (HDR) test site in the United States, in which the MS cloud did not extend to the σ_1 orientation (Norbeck et al., 2018). Tezuka & Niitsuma (2000) discussed the shape of the MS cloud of the Hijiori HDR test site, Japan, which had a biased distribution based on the existing fractures. These examples indicate that MS cloud growth behavior is very complicated and is not yet fully understood, especially in three-dimensional (3D) situations.

Recent studies have shown that microseismic analysis can provide a very detailed map of the fracture system using relocation techniques (Asanuma et al., 2008; Kraft & Deichmann, 2014). However, the phenomena associated with reservoir creation within an existing fracture system are too complicated in terms of relocation uncertainty and the potential effects of aseismic fracture. Therefore, we take a macroscopic approach to evaluating reservoir creation in terms of the MS cloud growth shape by attempting to clarify its relationships to *in-situ* stress, existing fracture distribution, and pore pressure. We utilize well-recorded microseismicity, *in-situ* stress measurements, and existing fracture data from the EGS project in Basel, Switzerland as a case study. Then, we discuss whether the insights from the analysis may explain the MS cloud growth behavior of other fields considering *in-situ* stress and existing fracture conditions.

2 Data and Methods

2.1 Field description

We studied microseismic activity observed at the EGS reservoir hydraulic stimulation project in Basel, Switzerland, in 2006. The EGS project aimed to create an artificial geothermal reservoir for electricity and heat supply as a co-generation system. Basel is located at the southern end of the Upper Rhine graben, characterized by having the highest geothermal potential in Europe (Baria et al., 1999; Charléty et al., 2007) (Figure 1). The injection well, Basel-1, was drilled in the urban part of the city to a depth of approximately 5000 m from the surface. A granitic basement was encountered below the upper sedimentary section with a thickness up to 2500 m. The casing shoe was installed to approximately 4630 m, and the remaining 400 m of the open-hole section was subjected to stimulation. Injected water penetrated the formation via several permeable zones in the open-hole section (Häring et al., 2008). Hydraulic stimulation was conducted for approximately five days, beginning on December 2, 2006. The maximum flow rate was 3300 L/min, accompanied by a wellhead pressure reaching 29.6 MPa (Häring et al., 2008). Injected water penetrated the formation via the cataclastic zone at the top of the open-hole section of the injection well, which was located at approximately 4670 m depth (Dyer et al., 2008; Häring et al., 2008). Hydraulic stimulation successfully caused numerous microseismic events. Seismic activity increased with the flow rate and wellhead pressure, and the MS cloud extended during the hydraulic stimulation process. On the fifth day of hydraulic stimulation, microseismic activity had risen to an undesirable level (Häring et al., 2008). Despite efforts to reduce the flow rate, seismic activity and following shut-in operation, several felt events, including the largest event (Mw 3.41), occurred during the shut-in phase (Häring et al., 2008; Mukuhira et al., 2013). Microseismic activity continued even after half a year following the termination of stimulation (Mukuhira et al., 2013), and seismic activity has continued until at least 2018 recent times (Herrmann et al., 2019).

2.2 Microseismic data

The primary operator of the EGS project, Geothermal Explorers Ltd. (GEL), installed a microseismic network consisting of six downhole seismometers and one sensor in the injection well (Figure 1). The deepest seismometer, Otterbach 2, was installed at the top of the granite section, and other seismometers were installed in the sediment. One geophone was deployed in Basel1 at 4720 m from the surface to capture the event signals at the very early stages of stimulation. The data from these events were used to calibrate the initial velocity model estimated from P- and S-wave velocities based on sonic velocity measurements, assuming that those events occurred within 100 m from the injection point. Following this, a one-dimensional and single layer (i.e., between sediment and granite) velocity model was used for hypocenter determination by GEL (Dyer et al., 2008).

The initial hypocenter was determined using the grid-based migration method with automatically detected P- and S-wave arrival, and events with a root-mean-squared (RMS) misfit of more than 10 ms were discarded (Dyer et al., 2010). Until the tenth day from the onset of stimulation, the microseismic monitoring system detected around 13500 triggers of potential events, whereby ~3100 events were located. Dyer et al. (2010) improved the determination of hypocenter locations of microseismic events by applying cross-correlation picking and multiplet analysis.

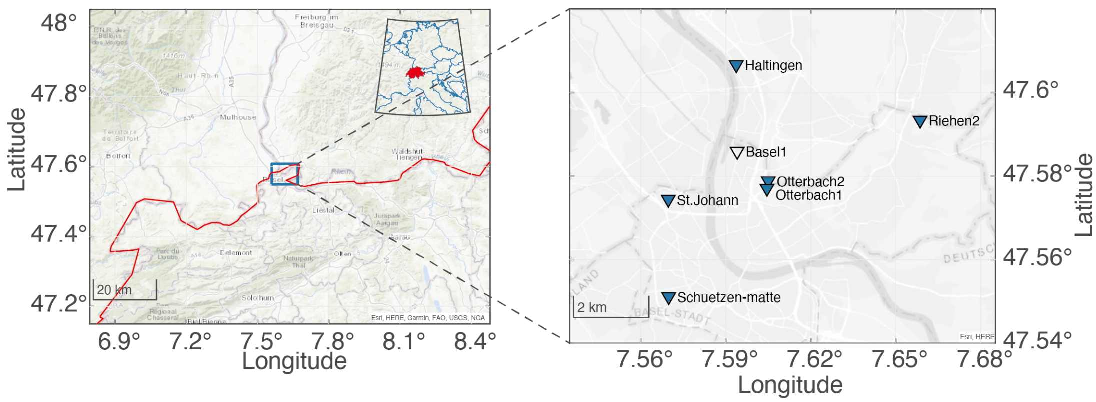

Figure 1. Location of Basel, Switzerland (left) and the microseismic monitoring network of the Basel EGS project in Basel City (right; blue triangles). The open triangle represents the location of the injection well, Basel-1.

In this study, we used the hypocenter locations determined by Asanuma et al. (2008). Asanuma et al. (2007; 2008) provided an independent analysis on the same microseismic data set used in Dyer et al. (2010). They manually picked the P- and S-wave arrivals and then determined the hypocenters, which were almost identical to those determined by Dyer et al. (2008). They also applied multiplet analysis (Moriya et al., 2002) to detect the relative time of arrival for P- and S-waves. Approximately 70% of microseismic events could be grouped into 100 clusters. Relocated clusters using a double difference method (Waldhauser & Ellsworth, 2000) delineated several sub-fractures in the reservoir (Asanuma et al., 2008). The spatial error in the absolute hypocenter locations was approximately 40 m, and the error in the relative hypocenter locations was less than 10 m. The error ellipsoids for hypocenter determination of each event were sub-vertical, showing at least 100 m of the longest axis. Residual distribution based on the monitoring network and velocity model showed a sub-vertical ellipsoid with robustness in terms of the resolution of hypocenter determination, although the vertical resolution was a bit lower than the lateral resolution (Asanuma et al., 2007). The MS cloud had a sub-vertical geometry striking in the NNW-SSE direction macroscopically.

In addition to the earthquake catalog used here and that from Dyer et al. (2008)other groups generated earthquake catalogs. Deichmann and Giardini (2009) and Kraft and Deichmann (2014) used the catalog based on regional surface networks. Kraft and Deichmann (2014) precisely analyzed microseismic data from downhole network and conducted relocation using a different frequency band and clustering algorithm to those of Asanuma et al. (2007). The overall shape of the MS cloud from Kraft and Deichmann (2014) was quite similar to that used in this study; thus, it was determined that discrepancies between the catalogs would not be a critical problem for the purpose of this study. Recently, Herrmann et al. (2019) detected more microseismic events occurring as recently as in 2018, using a matched filter technique at a single station, and providing detection time and magnitude.

Figure 2 shows an overview of the MS cloud in 3D for the stimulation period (until the shut-in). Microseismic activity began near the injection well and then expanded outward. Seismic activity near the injection well continued with the increase in flow rate. During the shut-in and bleeding-off phase (~5 d from the shut-in), pore pressure re-distribution occurred. This caused very active microseismic activity in the periphery of the previously stimulated region (see details in Mukuhira et al., 2017). However, the present study only focused on the stimulation phase since the interaction between pore pressure migration and the occurrence of microseismicity was clear in the stimulation phase.

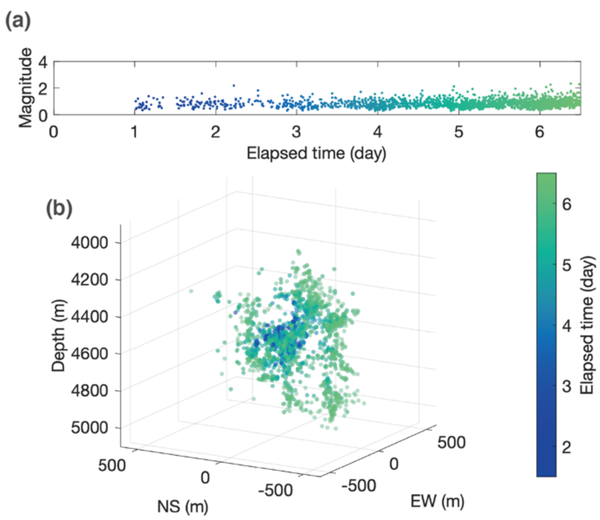

Figure 2. a) Magnitude-time (M-t) plot for the stimulation period. The color in the M-t plot indicates the elapsed time since the start of the stimulation for the microseismicity. b) Three-dimensional figure showing the hypocenter distribution of microseismic events with timing indicated by color. The color corresponds to the occurrence time of the events from the start of injection.

2.3 *In-situ* stress data and natural fractures

The orientation and magnitude of the *in-situ* stress in the study area were previously investigated using borehole logging data (Valley & Evans, 2009, 2015, 2019). Based on borehole breakout and drilling-induced tensile fracture data (Valley & Evans, 2009), the orientation of the maximum horizontal stress was estimated to be N144°E±14°. In previous studies (e.g., Mukuhira et al., 2018), we used the *in-situ* stress magnitude model proposed by Valley and Evans (2015). Recently, Valley and Evans (2019) revised the *in-situ* stress magnitude based on consideration of borehole breakout, drilling-induced tensile fracture, and several other failure criteria. The linear depth trends of stress magnitude proposed by Valley and Evans (2019) were $S_v=24.9z$, $S_{hmin}=7\times z + 42$, and $S_{Hmax}=5\times z + 90$, with the unit of stress being MPa and z being the depth in km from the surface. This small gradient, S_{Hmax}, led to the stress state transition at 4200 m from strike-slip to normal faulting below. The estimated *in-situ* stress model was consistent with the observed mix of strike-slip and normal fault-type focal mechanisms of larger induced seismic events (Deichmann and Giardini, 2009). We used this *in-situ* stress model, assuming a laterally homogeneous stress state in the reservoir region, for comparison with MS cloud growth and interpretation.

Several natural fractures were detected from borehole image data obtained with a Schlumberger Ultrasonic Borehole Imager (UBI), and those natural fractures were extensively analyzed (Ziegler, et al., 2015; Ziegler & Evans, 2020). At depth, the reservoir was dominated by NNW-SSE striking fractures, which is consistent with the current *in-situ* stress regime; however, a wide variety of natural fractures in the granite section were also present, including those striking NE-SW nearly perpendicular to the orientation of S_{Hmax} (Ziegler et al., 2015). Some of those fractures were identified in association with the fractures delineated by the microseismic cluster (Ziegler & Evans, 2020). Thus, natural fracture distribution provided the means to determine the potential orientation of existing fracture systems in the reservoir, suggesting that there was a variety of natural fractures consistent with the *in-situ* stress direction.

Rice (1993) proposed the following model of the stress-dependent permeability along each fracture: $k=k_0\exp(-\sigma_n/\sigma')$ where k is the permeability, k_0 is the permeability at no loading, σ_n is the effective normal stress, and σ' is the constant parameter to determine the decay rate of the permeability. Another model considering shear dilation was proposed by Willis-Richards et al. (1996) based on cubic law $k=a^2/12$, where the fracture aperture a is described as follows, $a= a_0/(1+9\sigma_n/\sigma'')+a_s$, a_0 is the fracture aperture at no loading, σ'' is the effective normal stress to cause 90% closure of aperture, and a_s is the change in aperture due to shear slip. Thus, permeability is influenced by shear dilation some extent. From these theories, the permeability of each fracture is the function of its geometry to *in-situ* stress, as well as the connectivity to other fractures, which is unknown.

2.4 Principal component analysis (PCA)

We employed PCA to the hypocenter location data of microseismicity in order to quantitatively and statistically characterize the MS cloud shape. PCA is a data analysis technique to characterize data distribution and can be applicable for the decomposition of high dimensional data to lower dimensions, and it has recently been used in unsupervised machine learning analysis (e.g., Shu et al., 2018). In general, PCA detects the basis along which the variance of the data distribution is maximized. In practice, principal components are computed by eigen decomposition of the data variance-covariance matrix, which, in this study, consisted of the hypocenter coordinates, and the principal components are considered eigenvectors of the covariance matrix. The variance of the microseismic hypocenter tends to be at its maximum along with the first principal component, meaning that the MS cloud's axis of largest extension is usually in the direction of the first principal component. PCA has also been used to evaluate the shape and orientation of seismic clusters (e.g., Mukuhira et al., 2013; Xue et al., 2018).

We applied PCA to microseismic hypocenters consisting of the MS cloud and then extracted the three principal components to characterize the MS cloud shape, assuming that the MS cloud grows from the point injection source, which is the case of EGS hydraulic stimulation. We define the data matrix **M** which consists of hypocenter location of the microseismic events in a time window.

$$\mathbf{M} = \begin{pmatrix} x_1 & \cdots & x_n \\ y_1 & \cdots & y_n \\ z_1 & \cdots & z_n \end{pmatrix} \qquad (1).$$

We extracted the three principal components to characterize the MS cloud shape, assuming that the MS cloud grows from the point injection source, which is the case of EGS hydraulic stimulation (for detail procedure, please see appendix). Note that we did not fix the centroid point of the hypocenter in PCA. The lengths of each component were computed from the eigen values $\mathbf{\Lambda}$ as they are the maximized variance of the data along with each principal component, and then we used the square root of variance (standard deviation) that were increased by a factor of three. Effectively, three orthogonal principal components can model the MS cloud as an ellipsoid defined by the components' directions and lengths. The resulting ellipsoid should include 99% of microseismic events. Note that we did not intend to model the MS cloud as an ellipsoid, but we did intend to characterize the MS cloud shape with PCA. The uncertainty of each hypocenter location should not affect the PCA results because PCA evaluates the whole data distribution. In other words, one event with high uncertainty would not influence the PCA results. Moreover, the error ellipsoid shape for each event in the reservoir was similar and the longer axes were oriented in the vertical direction (Asanuma et al., 2007), suggesting that any event from a particular region in the MS cloud would not have an influence on the PCA results. It should be noted that the principal components in this analysis were defined as left-handed coordinate systems.

3 Analysis

3.1 Three-dimensional MS cloud growth

First, we focused on MS cloud growth during the stimulation period, from the start of the stimulation to the time of the shut-in. We computed the three principal components of the MS cloud every 0.5 days. The MS cloud of each time step included all microseismic events occurring prior to the target time. Figure 3 shows the 3D microseismic distribution for each time step and the ellipsoids defined with three principal components. The distribution of microseismic events changed with time; however, the ellipsoids shown in Figure 3 did not change significantly. The first PCA component (depicted by red) was more horizontal in the early few days and commenced dipping around 45° from the horizontal on the third day. The first and second principal components sometimes switched by 180° according to the local and temporal progress of the MS cloud. The 180°-transition of each PCA component posed no issue in terms of its relationship with the MS cloud growth and *in-situ* stress due to the symmetry of the *in-situ* stress. The first and second principal components switched directions at 4.5 and 5 days. At the last time step of 6.5 days, the orientation of the first and second principal components showed different behavior compared to that prior to that time step during stimulation as follows. The first PCA component dipped in the NW direction at first, but then became more vertical at 6.5 days, and the second PCA component stayed close to vertical, which is more evident in Figure 4(a)–(b). It should be noted that the wellhead pressure increased gradually until the 6th day and then decreased due to flow rate reduction from 6 to ~6.5 days.

The orientation of the computed principal components is summarized in the lower hemisphere plot in Figure 4(a)–(c), which represents the time series change of the MS cloud growth orientation. We observed that in the third principal component, the minor orientation of MS cloud growth was constant and almost identical to the minimum horizontal stress, S_{hmin}. In contrast, the first and second principal components changed in the plane perpendicular to the orientation of S_{hmin}. Figure 4(d) shows the time series changes of each principal component length, while Figure 4(e) shows the aspect ratio for the first and second principal components to the third one. The first and second principal components were nearly similar values throughout the stimulation period shown in Figure 4(d). In contrast, the third principal component grew to 120 m at most; this was around one-fourth the length of the first and intermediate principal components. The aspect ratios between components varied together between 2.5 and 4. The PCA results for the incremental time step is shown in Figure S1; the results are almost the same as those shown here.

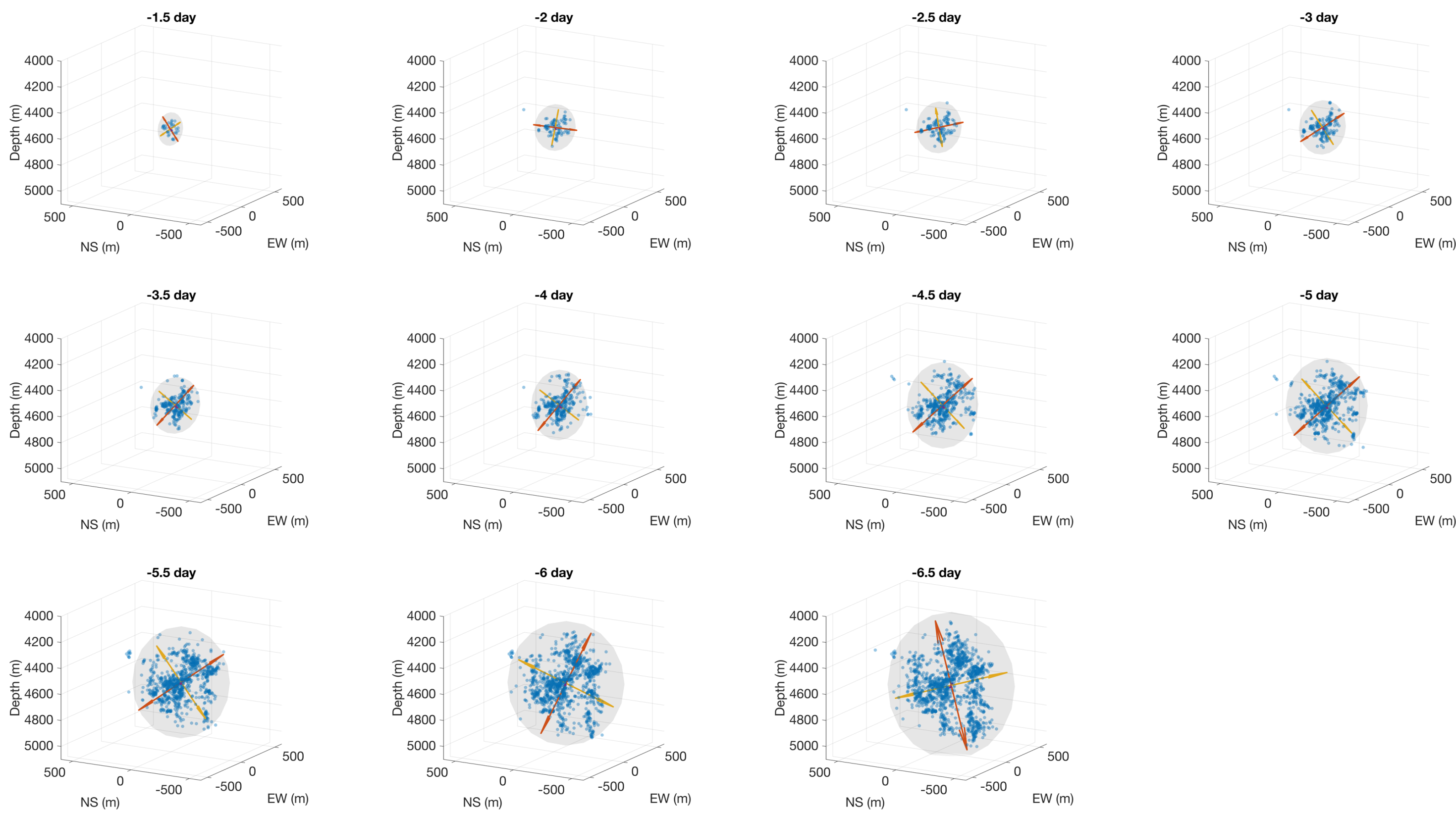

Figure 3. Snapshots of the 3D hypocenter distribution of microseismic events were taken every 0.5 d from the start of the stimulation. The red, yellow, and purple arrows correspond to the first, second, and third principal components that describe representative ellipsoids for MS clouds at each time. Note that purple arrows are hidden by the markers for hypocenters and they are inherently small.

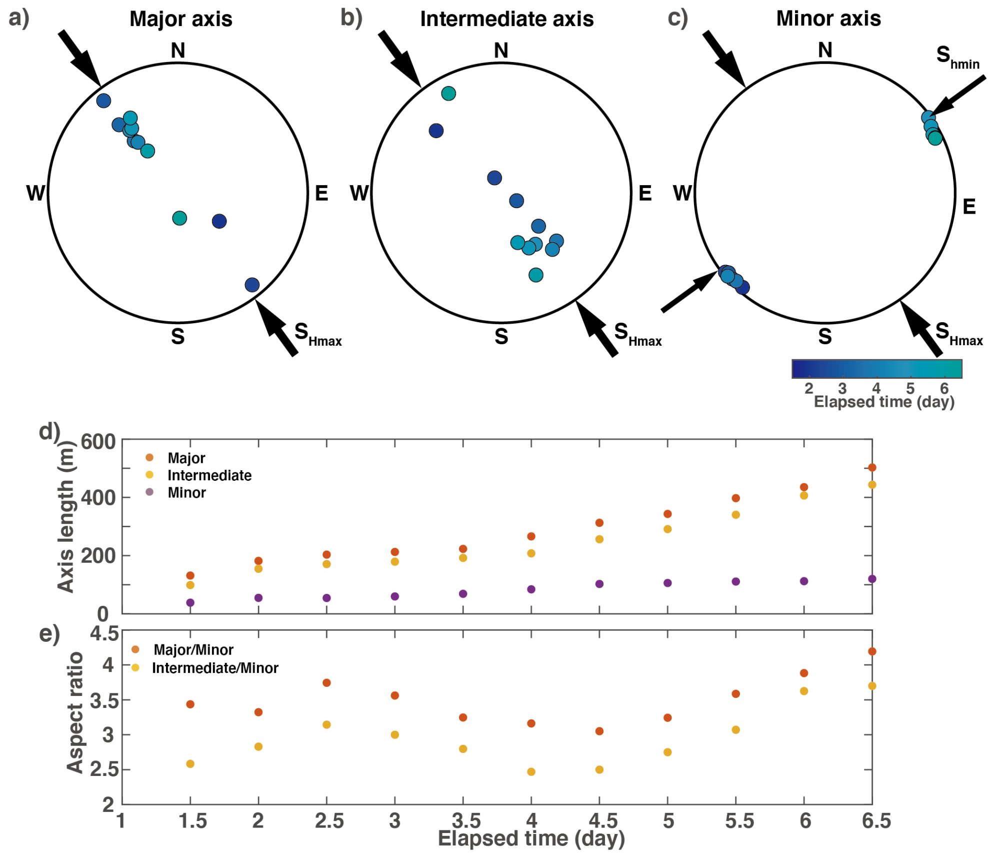

Figure 4. Time series change of first, second, and third principal component vectors: a) major; b) intermediate; and c) minor axes orientation for representative ellipsoids in the lower hemisphere projections. The presented principal component vectors are the same as those shown in Figure 3; d) time series for change of principal component length (major, intermediate, and minor axes lengths); and e) the aspect ratio between the first to third principal component lengths (red) and second to third principal component lengths (yellow).

3.2 Depth sectional of MS cloud growth

We investigated the MS cloud shape further at different depths and examined the influence of depth-dependent *in-situ* stress and possible pore pressure gradient by depth. We applied PCA to microseismic events from a 100 m width different depth section. We computed only two principal components, ignoring the depths of each microseismic event. No depth sections for this analysis overlapped, and microseismic events that occurred from the same vertical existing fault were contained over several depth sections. In addition to the principal components, the geometric relationship between the centroid point of the selected MS cloud to each hypocenter is summarized as a rose diagram in a subset for each panel of Figure 5.

We observed a linear MS cloud shape in the shallower part of the reservoir (4000–4200 m), where almost no variation in the orientation of fracture failed at this depth. From ~4200 m, we observed that the MS cloud had begun to thicken owing to events occurring in different fractures. These features resulted in the extension of the second principal component and an elliptical shape for the entire MS cloud. This tendency was especially observed in the MS cloud at deeper depths (4200–4700 m). In the 4300–4400 m depth section, the MS cloud was very sparse, and the rose diagram shows very different shapes to those at shallower depths. Seismic activity was observed in branch fractures striking E-W at 4400–4500 m. At this depth, the northern MS cloud appeared independent of the main and southern parts of the MS cloud. In the next depth section of 4500–4600 m, the densest seismic activity moved slightly north, as demonstrated by the centroid point of the MS cloud. In the deeper part of the reservoir, the MS cloud could be divided into northern and southern parts according to its seismic and aseismic regions.

Despite the depth-dependent features of microseismic activity and associated MS cloud shape, the macroscopic trend of the MS shape was maintained as the MS cloud extended in an orientation almost identical to S_{Hmax}. Figure 6(a) summarizes the azimuths of the first principal component variation and depth and shows that the azimuth of the first principal component had slightly rotated from N-S to NW-SE with an increase in depth. This rotation should be attributed to the difference in microseismic activity at each depth. We visualized the existing fractures delineated by multiplet analysis (clustering analysis) at each depth in Figure S3. The aspect ratios of the MS cloud at each depth were between 2 and 4, with the exception of those at depths at 4700–4800 m, as shown in Figure 7. At shallower depths, the aspect ratios exceeded 6; these exceptionally high aspect ratios reflect the linear shape of the MS cloud at shallower depths. It should be noted that the majority of the events from ~4200 m occurred following the shut-in operation.

Because we investigated the MS cloud shape in different depth sections, we estimated the horizontal stress ratio, defined as $(S_{Hmax}-p_{hyd})/(S_{hmin}-p_{hyd})$, for each depth (Figure 7(b)), where p_{hyd} is hydrostatic pore pressure. The horizontal stress ratio in the reservoir depth was approximately 2.3. The horizontal stress ratio was not a bit smaller than the aspect ratio of the MS cloud, although it was fairly consistent with the aspect ratio of the MS cloud growth except for the two shallow sections.

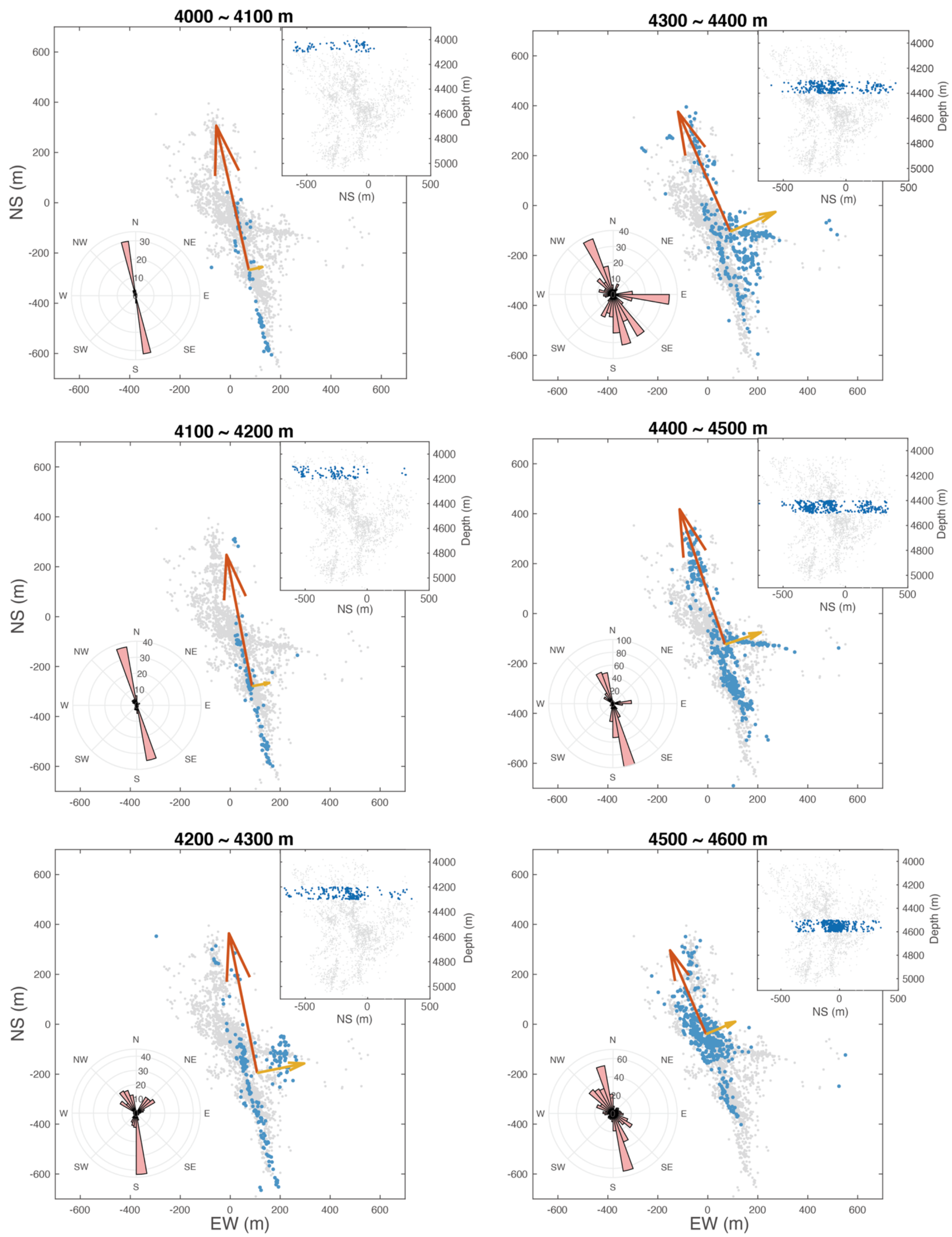

Figure 5. Hypocenter distribution of events for different 100 m depth sections in horizontal view. The blue dots are the event hypocenter in the target depth. The results of the two-dimensional (2D) PCA are shown with two arrows. The upper right inset is a N-S cross-section showing the target depth. The gray dots denote all microseismic events. The left lower inset

represents the rose diagram for geometrical orientations from the centroid point of target events to each event.

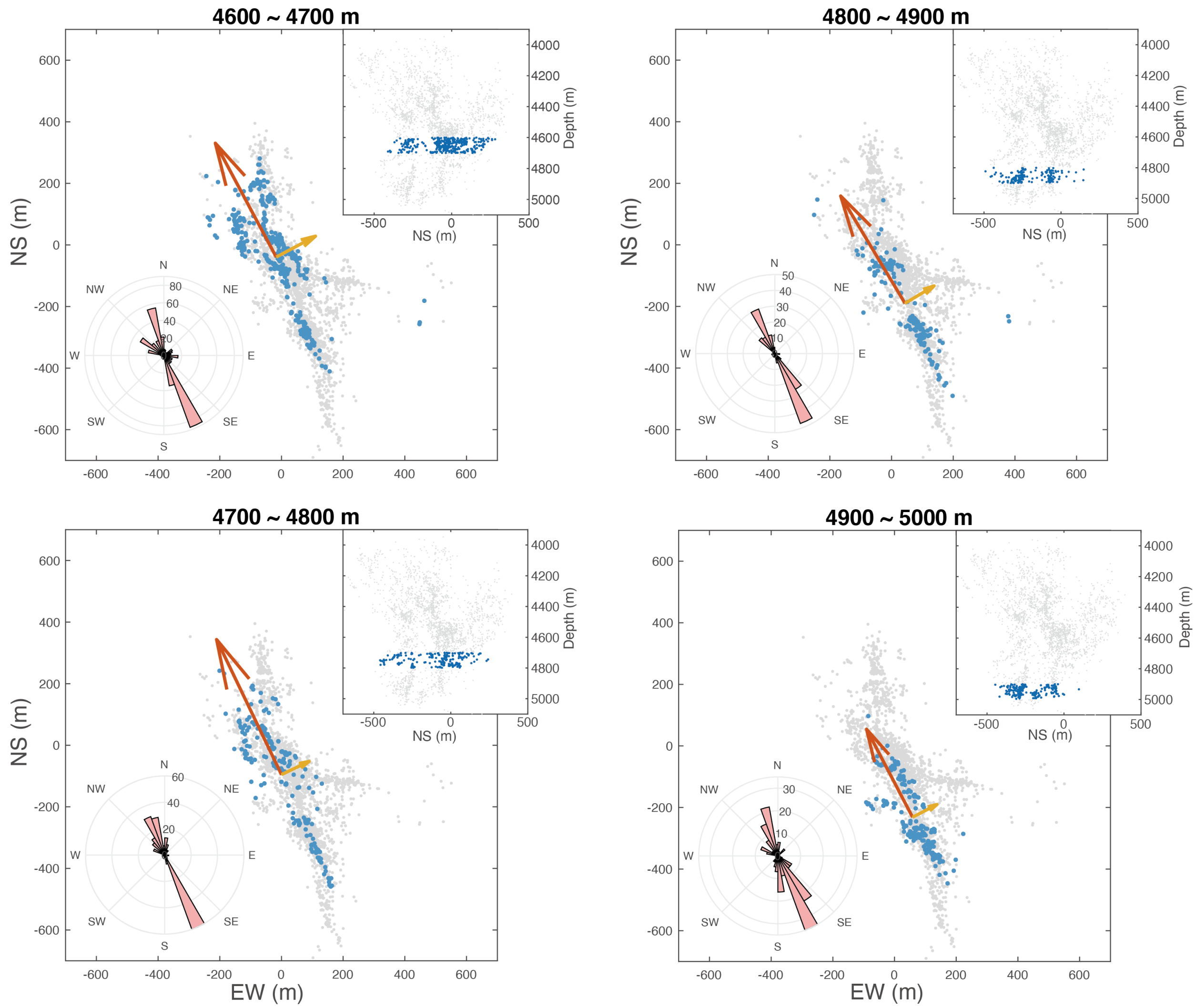

Figure 5. (continued).

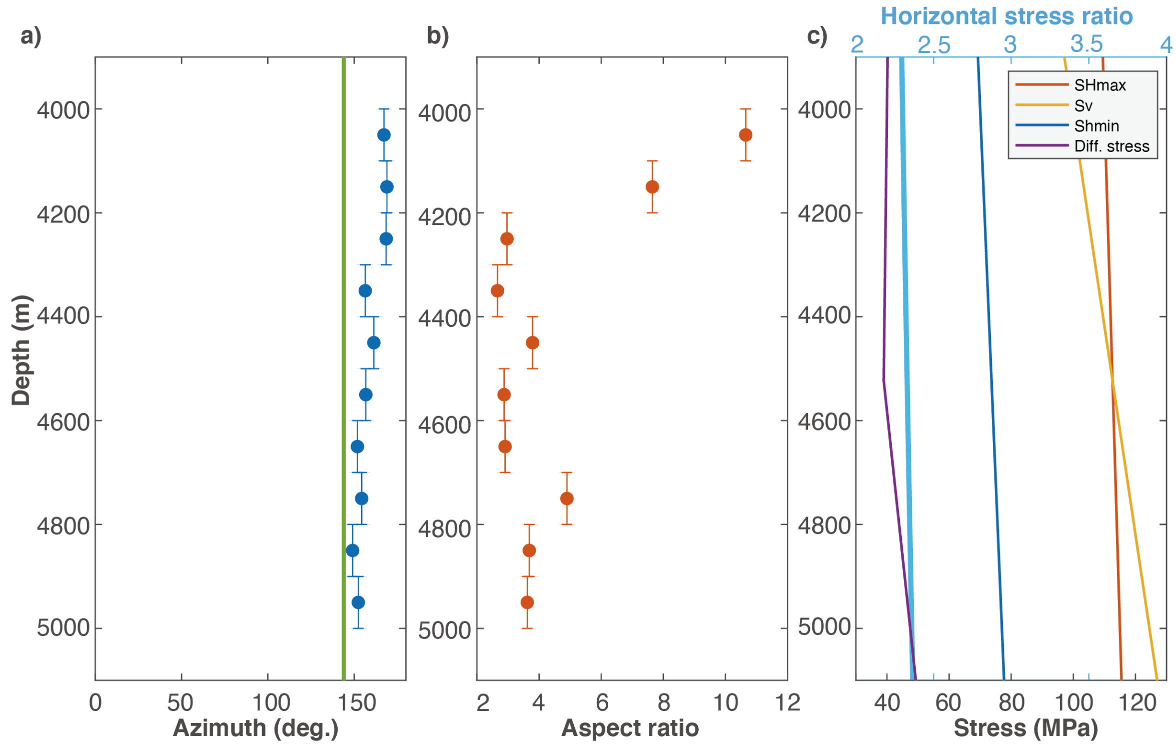

Figure 6. a) Orientation of the first principal component as a function of depth. The vertical bar indicates the depth of the analyzed section, while the vertical green line shows the orientation of S_{Hmax}; b) aspect ratio between the lengths of the first and second principal components; and c) the stress profile in study depth with horizontal stress ratio $(S_{Hmax}-p_{hyd})/(S_{hmin}-p_{hyd})$.

3.3 Injection depth MS cloud growth

During injection, the injected pore pressure migrates from the feed point in the well through the formation (Häring et al., 2008). The pore pressure decays with distance from the injection point based on the permeabilities of existing fractures of the flow path, their connectivity, and the injection pressure. Thus, pore pressure migration is a complicated and nonlinear phenomenon. It may be reasonably assumed that either the pore pressure in the vicinity of the injection point was as high as that at the bottom well, or the pore pressure decay was relatively small. Therefore, we may forecast that the MS cloud shape near the injection point was linear or simple during the initial stage of stimulation, as only the well-oriented fractures are likely to experience shear failure. Later, the more non-optimally oriented existing faults may cause shear slip as the pore pressure increases, making the MS cloud more spherical in shape. Based on this concept as a working hypothesis, we further investigated the time series change of the MS cloud shape at the injection depth.

We focused on an event that occurred between 4500 and 4700 m, which included the feed point (4681 m) of the cataclastic zone (Häring et al., 2008). The microseismic activity started from this depth at the start of the stimulation (Figure 7, ~1.5 day panel). We focused on NS > -200 m as we observed that the southern part of the MS cloud was divided by the aseismic zone and not directly connected to the injection zone as we discussed in 3.2 (Figure 6). We applied 2D PCA to a time series of MS cloud growth at every 0.5 d (Figure 7). The MS cloud had been drop-shaped, linearly extending to NW and forming an elliptical or circular shape near the injection point until 3.5 days of the stimulation. After 3.5 days, the MS cloud became thicker with time, and its shape became more elliptical. The incremental time analysis result is shown in Figure S4.

The relative geometry from the MS cloud centroid point is summarized in Figure 8(a) in the same manner as Figure 6. The rose diagram shows the orientation range of the MS cloud shape as it became wider over time (according to pore pressure increase). The rose diagram shape varies somewhat, suggesting that more events occurred in the northern direction. The time series change in the first and second principal components and their lengths are summarized in Figure 8b. The orientation of the first principal component was more or less stable during stimulation. Therefore, the macroscopic MS cloud growth orientation was relatively preserved despite the change in the MS cloud shape. The aspect ratio increased gradually, reflecting a more linear MS cloud shape during the early stage of the stimulation. After 2.5 days, as we forecasted and observed in Figure 7, the aspect ratio of the MS cloud shape decreased, representing that the MS cloud became thicker. Consequently, the aspect ratio decreased from 3.5 to 2.5. Note that the effective horizontal stress ratio at this depth was approximately 2.34.

The contribution to the whole MS cloud shape from each existing fracture is delineated with the microseismic clusters in supplementary Figure S5; the interaction among each existing fracture was difficult to see due to complexity.

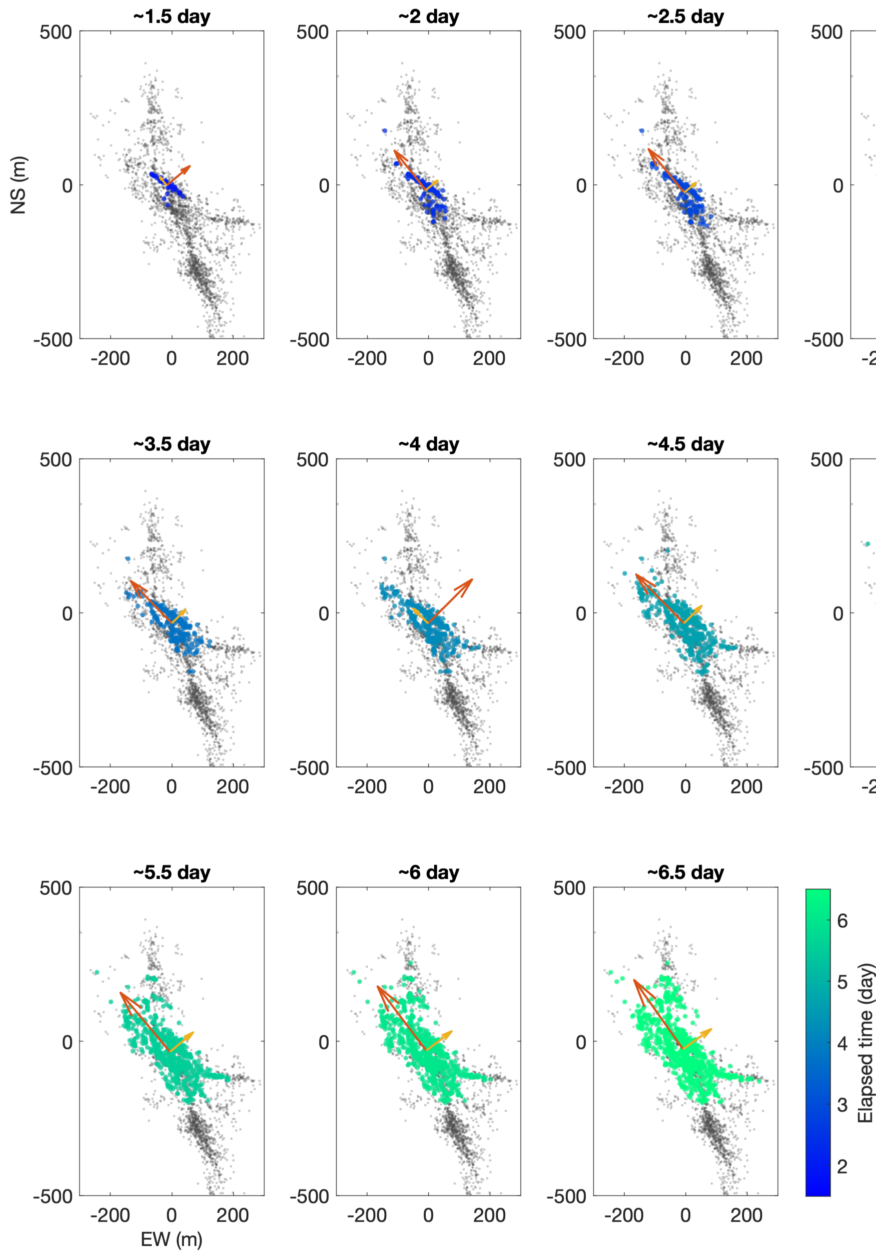

Figure 7. Time series evolution of microseismic events at an injection depth of 4500–4700 m. The 2D PCA results are depicted with two arrows; red: first component, yellow: second component.

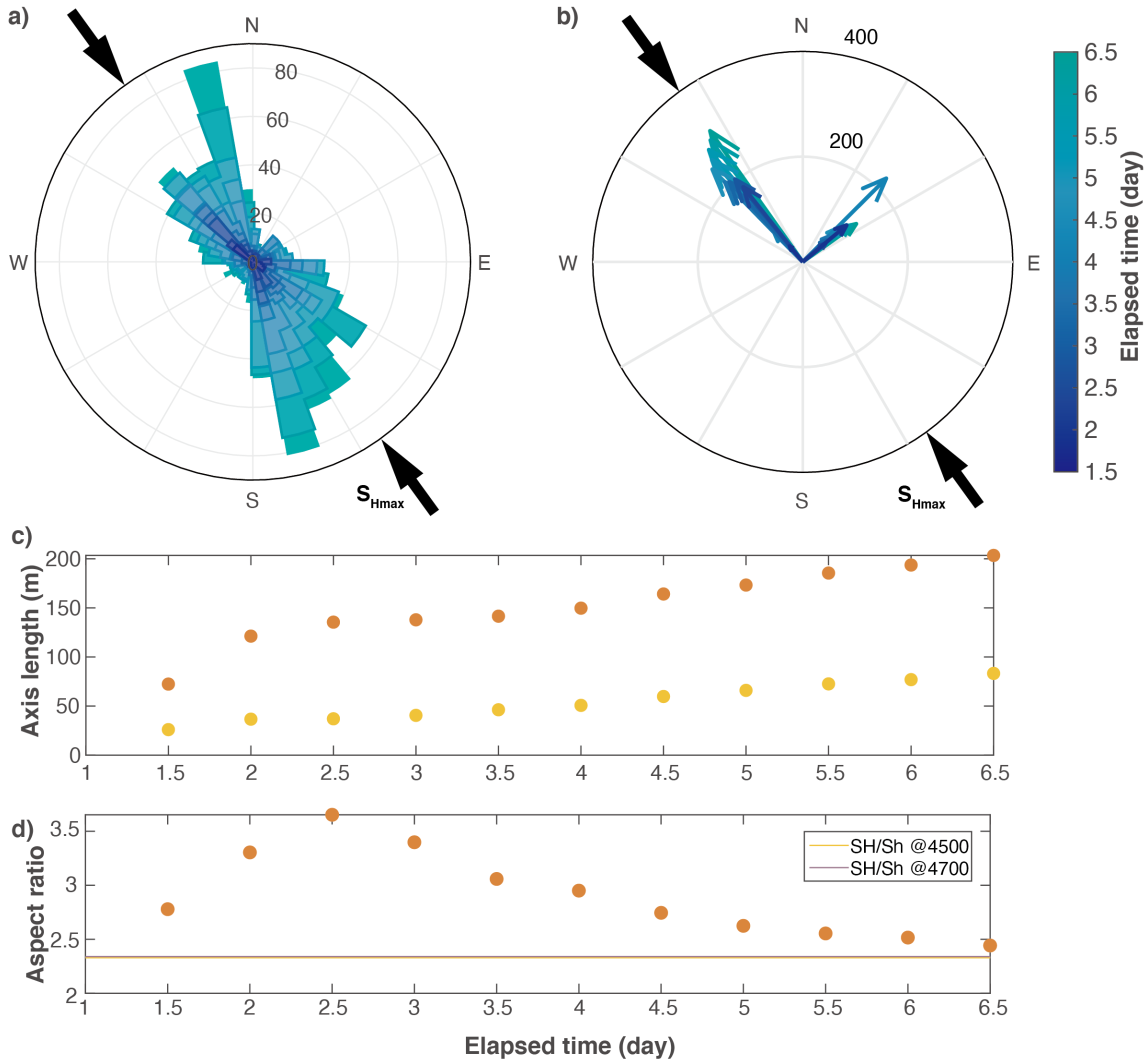

Figure 8. a) Rose diagram of geometrical orientations from the centroid point of each event, with the color of the rose diagram corresponding to the analysis time; b) time series change of orientation and length of the first and second principal components, again with the color corresponding to the analysis time; c) length of first and second principal components as a function of time; d) aspect ratio of first and second principal components as a function of time compared with the horizontal stress ratios at 4500 and 4700 m.

3.3 Cross-sectional MS cloud growth

We observed the cross-sectional MS cloud growth along the orientation of N144°E (N36°W), which is the same orientation as that of S_{Hmax}, and to correlate with *in-situ* stress, we chose the principal stress coordinate. This choice is reasonable based on the PCA results presented in Section 3.1. Figure 9 shows the time series evolutions of the MS cloud along the N36°W cross-section. For this analysis, we selected events that occurred within ± 200 m from

N36°W (Figure S6). The incremental time series analysis is shown in Figure S7, and the multiplet analysis results are shown in Figure S8.

In the first three time steps up to 2.5 days, the first principal component was nearly vertical (inclination < -80), and the lengths of both the first and second principal components were close to each other (aspect ratio was around 1.2). On the 3rd day, one of the components started dipping. The lengths of the first and second principal components continued to be nearly the same so that they both switched at 3.5, 4.5, and 6 days. The principal components showed different behavior at the time step of 6.5 days, in that the first principal component was oriented nearly vertically. These observations are basically the same as those of the 3D observations presented in Section 3.1. We visually confirmed that the MS cloud grew symmetrically, and that the MS cloud shape was more or less circular (Figure 9). The aspect ratio was between 1–1.3, and was more stable than that in the case of depth sectional analysis (Figure 10(a)). The ratio between S_{Hmax} and Sv was 1–1.15 in the target depth section (4200–5000 m), showing very good agreement with the MS cloud growth aspect ratio, even though the stress transition occurred from the strike-slip regime to the normal fault regime at around 4500 m (Figure 10(b)).

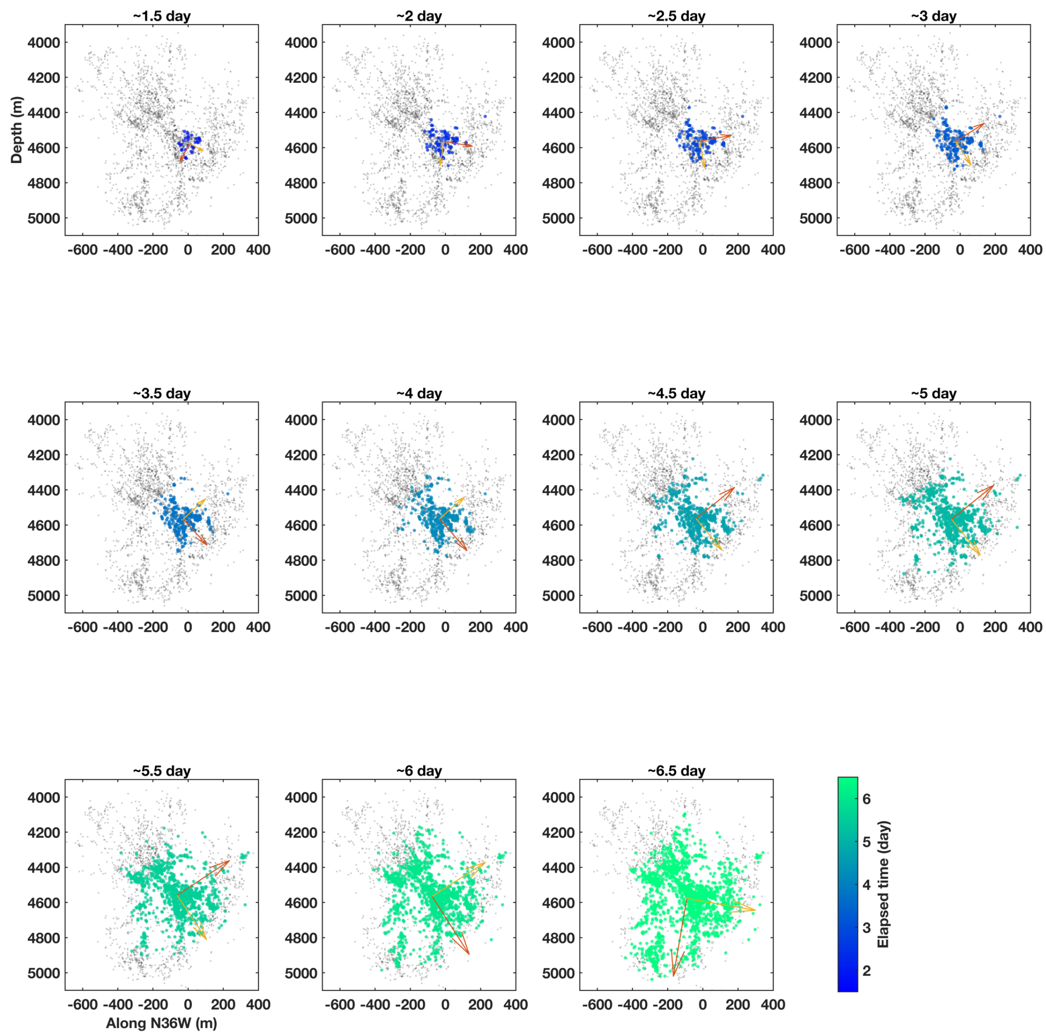

Figure 9. Time series evolution of microseismic events along the N35°W until 6.5 days from the start of the stimulation. Events that occurred within ± 200 m along N36°W were plotted and analyzed. The 2D PCA results are depicted with two arrows; red: first component, yellow: second component.

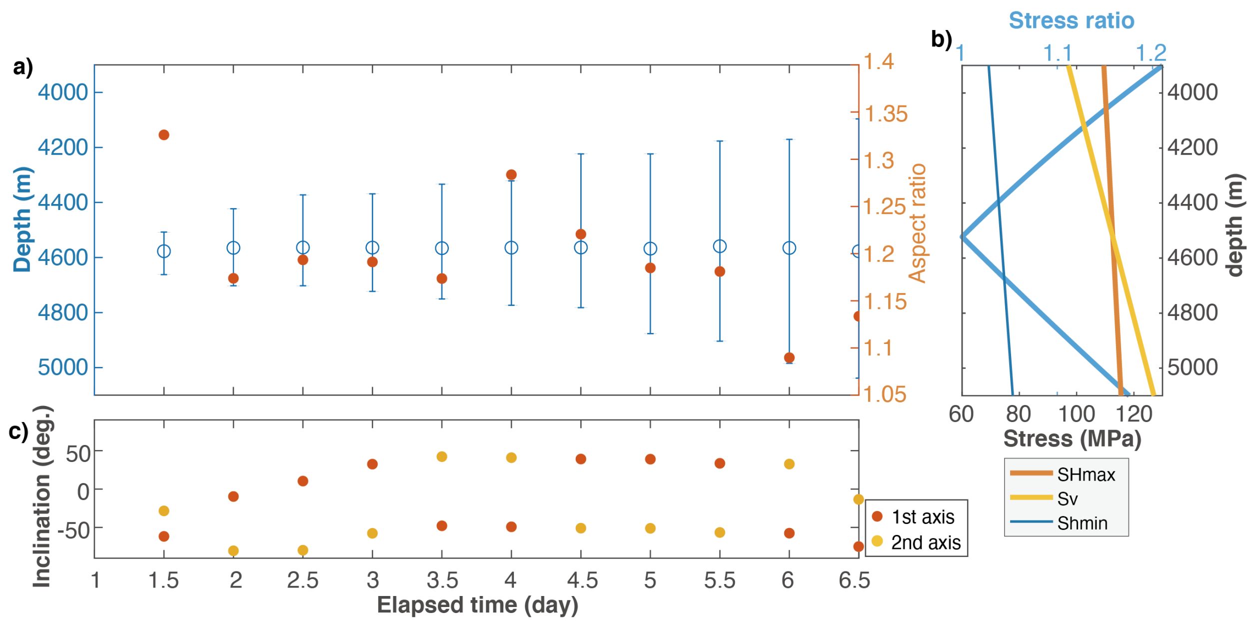

Figure 10. Correlation between MS cloud shape and *in-situ* stress. a) Circles correspond to the centroid depth of the MS cloud, and the error bar corresponds to the upper and lower limits of the MS cloud. Red dots show the aspect ratio of the first and second principal components of the MS cloud. b) Stress profile and stress ratio between the vertical and maximum horizontal stress. c) Inclination of the first and second principal components. The downdip is negative in this figure.

4 Discussion

4.1 MS cloud growth controlled by *in-situ* stress

From the PCA results and all observations of the 3D MS cloud analysis, depth sectional analysis, time series of injection depth MS cloud data, and other MS cloud data, along with the determination of the largest and intermediate principal stress, we found that the MS cloud shape in our research field was mainly controlled by *in-situ* stress from the macroscopic perspective and that the MS cloud shape can be scaled with the *in-situ* stress ratio.

4.1.1 Orientation of MS cloud

The minor principal component was constantly oriented in the S_{hmin} direction, regardless of the scale change of the MS cloud over time (Figures 4 and 8). This suggests that MS cloud growth behavior in this field is a scale- and time-independent process, and that this process has macroscopic continuity over the reservoir. This observation also indicates the homogeneity of *in-situ* stress in the reservoir.

Meanwhile, the MS cloud extension did not always occur in the σ_1 direction in a simple manner. Instead, it occurred in the plane perpendicular to the σ_3. The orientation of the first and second principal components varied and sometimes flipped according to the pore pressure distribution. These phenomena should be attributed to the competition of the maximum and intermediate principal stress magnitudes depending on the depth in the field. Therefore, the influence of intermediate stress could not be ignored. From 2D MS cloud growth observations, the MS cloud extension orientation was more or less constant and consistent with the orientation of S_{Hmax} for different depths and time (Figures 6 and 8) despite the influence of various existing faults in each depth section and time dependent pore pressure distribution.

Previously, the MS cloud was considered to extend in the direction based on the mesh-like fracture system. Although this is partially correct compared to our observations, the MS cloud did not extend exactly to the σ_1. Sibson (1996) discussed the permeability which was preferably developed in the direction of the intermediate principal stress in the fracture mesh model. This interpretation is also partially correct. The MS cloud aspect ratio from depth sectional analysis in Figure 6 shows that the aspect ratios in the normal fault stress regime (around 4500 m) of the MS cloud seem to be larger than those in strike-slip stress regime (4200–4500 m). However, the fracture systems in this field and in the real world are much more complicated than the conceptual model. Consequently, all principal component directions are nearly identical to the directions of principal stresses. The largest principal component was sub-vertical, which is consistent with the maximum principal direction in the deeper part of the reservoir. Note that the 3D PCA results showed different MS cloud growth behavior at the last step of stimulation, which caused the first principal component to be vertical.

4.1.2 Scaling of MS cloud shape

We evaluated the MS cloud shape by comparison of the aspect ratios estimated from each principal component and the *in-situ* stress ratio. The 3D MS cloud aspect ratios showed that the major and principal intermediate components were very close in normalized scale to the minor principal components. This is qualitatively consistent with the *in-situ* stress magnitudes and their ratios. This was also confirmed in the 2D MS cloud shape cross-section along the maximum horizontal stress direction, in which we observed that the MS cloud aspect ratio was nearly identical to the stress ratio between S_{Hmax} and Sv. The 2D MS cloud aspect ratios at different depths should reflect the pore pressure distribution. In the reservoir depth section (4200–5000 m), the horizontal stress ratio was nearly constant. However, the MS cloud shape ratio tended to be larger than the horizontal stress ratio. Meanwhile, the MS cloud shape at shallower depths was strongly linear, posing a higher aspect ratio. The microseismic events from shallower depths were induced after the shut-in (Mukuhira et al., 2017). A tiny perturbation of pore pressure triggered these events, such that the delineated MS cloud showed the optimally oriented fractures. These are the faults on which shear slip is induced by relatively small pore pressure increase. Thus, the shape of the MS cloud is also influenced by pore pressure migration, in addition to *in-situ* stress. The same tendency was also observed in 2D MS cloud shape observations near the injection depth. The MS cloud shape was more linear at the early stage of stimulation as the pore pressure remained low, and optimally oriented faults experienced shear failure. Then, the MS cloud shape became more elliptical with time, i.e., the pore pressure increased because the non-optimally oriented fault could fail. Figure 8(d) shows a clear tendency that the aspect ratio of the MS cloud decreased with time, i.e., with pore pressure. It can be said that the pore pressure perturbation or existing fracture affects the MS cloud shape locally; moreover, the entire MS cloud shape can be controlled by *in-situ* stress. We did not explore the local interactions in detail as it was nearly impossible to link them to physical processes associated with microseismic activity and *in-situ* stress (e.g., multiplet cluster analyses in Figures S5 or S8), nor would this be very informative for our purpose due to its complexity.

According to the borehole measurements, critically stressed fractures (well-oriented fractures) have higher permeability because of relatively less normal stress and possible shear dilation in the past (Barton et al., 1995; Ito & Zoback, 2000). This is not entirely the same as the permeability prediction as a function of normal stress (Rice, 1992) but can potentially be explained in terms of the other form of permeability prediction by Willis-Richards et al. (1996), as discussed in Section 4.2, although evaluation of past shear dilation is very difficult. We computed the effective normal stress, delta pore pressure necessary for shear slip, and permeability at the injection depth of 4600 m based on the *in-situ* stress model. Permeability is predicted using the equation by Rice (1991), where we assumed $k_0=4\times10^{-16}$ m^2 and $\alpha=10^{-1}$ following Miller (2015). Note that this permeability estimation is for one independent fracture. In this computation, the effect of shear dilation is not considered; therefore, the most permeable fracture is considered to be the one perpendicular to the σ_3 direction due to the minimum effective normal stress (Figures 11(a) and (c)). The permeability of the fracture perpendicular to the σ_3 orientation is higher than that of well-oriented fracture by a factor of 2.74 in the case of the injection depth (Figure 10(c) and Figure S9). Therefore, the MS cloud extension in the direction of S_{Hmax} in the horizontal dimension, which overran the prediction from the *in-situ* (horizontal) stress ratio, can be interpreted with permeability differences between the fractures of the flow path. While the MS cloud can extend somewhat along well-oriented fractures, it can extend more easily along the fracture perpendicular to S_{hmin} regardless of the shear slip. Meanwhile, in this field, various natural fractures were determined according to borehole logging analysis (Ziegler & Evans, 2015). Some of these fractures were identified as those delineated by microseismic analysis (Ziegler & Evans, 2020). Some of the existing fractures were oriented in the direction of S_{hmin}. According to the fracture permeability evaluation, the fracture with the lowest permeability, which is perpendicular to σ_1, had a permeability nearly two orders of magnitude lower than that with the highest permeability (Figure 10(d)). Hence, we can consider that fractures perpendicular to σ_1 are practically impermeable even though they do exist. Therefore, the MS cloud growth in the σ_3 direction is attributed to the well-oriented fractures and other fractures that caused shear slip, rather than the fractures perpendicular to σ_1.

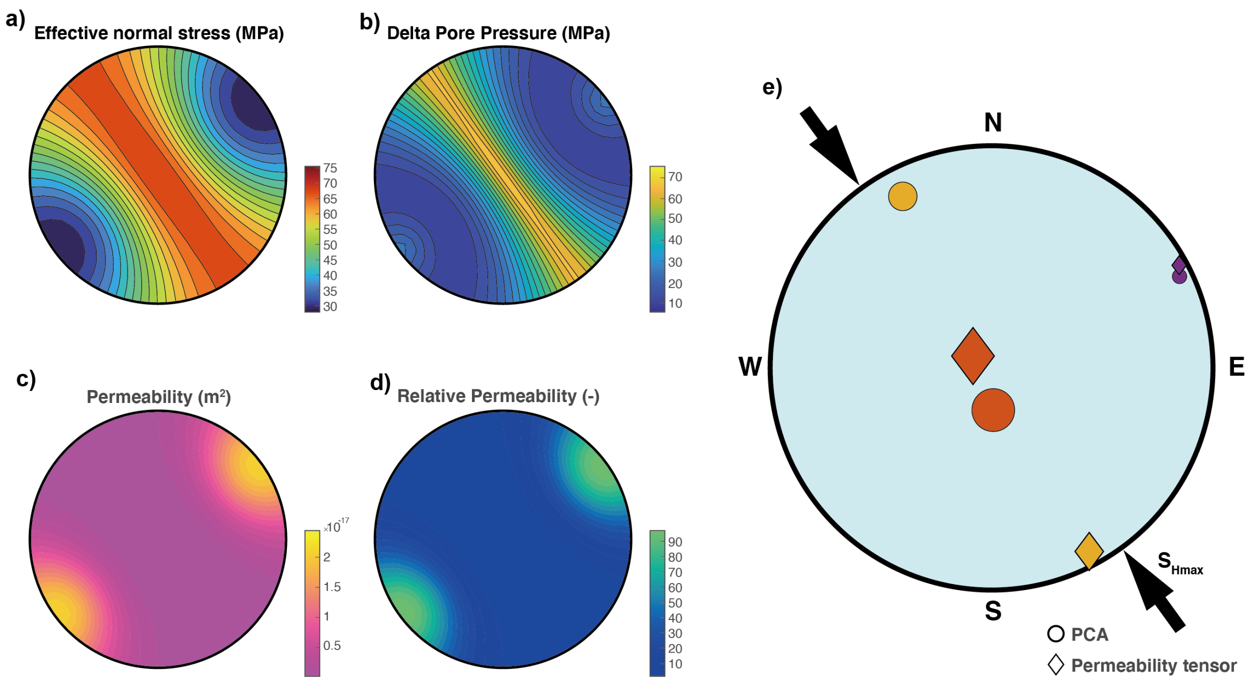

Figure 11. Distribution of (a) effective normal stress, (b) delta pore pressure for shear slip, (c) predicted permeability, and (d) relative permeability to the poles of arbitrary fractures, based on the in-situ stress model at 4600 m. (e) Comparison between PCA results of MS cloud growth (circles) and permeability tensors (diamonds). Red: major, yellow: intermediate, and purple: minor components or tensors.

4.2 MS cloud growth and permeability tensor

We empirically determined the possible scaling relationship between the MS cloud shape and *in-situ* stress; however, the physical relationship between them could not be determined. Therefore, we pose the question: can MS cloud shape be scaled with *in-situ* stress? To address this new and challenging question, we introduce the concept of permeability tensor. Microseismic events are triggered by pore pressure increase, which is controlled by pore pressure migration. Therefore, pore pressure migration behavior should be governed by the matrix permeability of the reservoir, which should be anisotropic, as the MS cloud shape shows. Matrix permeability can be considered as the aggregation of fracture permeabilities of each existing fracture in the system. The fracture permeability is the function of effective normal stress (discussed in Section 2.3). Thus, we estimate the matrix permeability tensor at the time of stimulation for the reservoir. Note that the natural matrix permeability tensor was altered by shear dilations associated with fluid injection, and we consider the apparent matrix permeability tensor as the permeability tensor which is achieved by hydraulic stimulation.

To estimate matrix permeability, we used the method proposed by Shapiro et al. (1997; 1999). In their methods, a 3D diffusivity tensor was determined along with three orthogonal principal bases. Then, a diffusivity tensor was converted to a permeability tensor. We applied their method to our microseismic dataset during the injection period and obtained a diffusivity tensor as $\boldsymbol{D}$= (0.48×10^{-1}, 0.31×10^{-1}, 0.48×10^{-2}) [m^2/s] and permeability tensor as $\boldsymbol{K}$=(5.43×10^{-17}, 3.48×10^{-17}, 5.41×10^{-18}) [m^2]. The orientation of the permeability tensor was compared with the PCA result at the end of stimulation (Figure 11e). Directions of the estimated permeability tensor showed a very good match with the orientation of the principal components. Furthermore, their magnitude relations were also consistent with the PCA results. The largest and intermediate permeabilities were quite close (at least in the same order of 10^{-17}), and they are 1 order of magnitude higher than the smallest permeability. It is not so surprising that no significant difference has emerged between largest and intermediate bulk permeability in consideration of the magnitudes of *in-situ* crustal stress in Basel. Such an anisotropic permeability tensor can be estimated form Nasseri et al. (2014), where they have reported the 3-D directional permeability during true-triaxial deformation experiments. They showed that the anisotropy of bulk permeability of microfracture networks associated to the magnitude of principle stress is less than 1 order of magnitude, though the correspondence between the directions of minimum/maximum permeability and of minimum/maximum principal stress was not as clear as our field observation. Note that, in the case of a single fracture, the fractures perpendicular to the maximum and intermediate principal stress are potentially impermeable, whereas the fractures perpendicular to the minimum principal stress are the most permeable. On the other hand, the anisotropic permeability tensor is given for the equivalent continuum with respect to the discrete fractures system. There is no doubt that the spatio-temporal evolution of the permeability tensor can closely relates to the MS cloud growth behavior in fractured systems, but it is strongly constrained by the preexisting fracture system after all. Thus, to derive their qualitative physical link, further observation and systematic numerical experiment are necessary to be collected.

4.3 Comparison with other EGS fields

In this section, we discuss how the insights derived from this study may explain the MS cloud growth in other past cases of EGS fields, although reliable *in-situ* stress measurements and microseismic analysis were not always achieved. We selected eight cases of EGS and HDR projects and reviewed the MS cloud growth features by comparing the *in-situ* stress information based on published literature. The reliability of microseismic and *in-situ* stress information is highly site dependent, and the project year also impacts reliability based on the available technologies at the time. All available information related to MS cloud shape and *in-situ* stress are summarized in Table 1. The details of each field are documented in the supporting information.

The MS cloud of the Soultz-sous-Forêts EGS (France), 1993 showed the most consistent characteristics to our field, likely owing to the Soultz field being part of the Rhine graben. There were stress consistent existing fractures, and they were mainly stimulated. Other EGS fields such as Desert Peak (United States), Helsinki (Finland), Hijiori (Japan), and Ogachi 2nd (Japan) also showed consistent features in that their MS clouds extended along the orientation of σ_1. However, the MS cloud shapes did not always conform to the *in-situ* stress ratio for some fields, such as Helsinki, which, in that case, was probably due to the non-point source injection caused by multi-stage stimulation and packer leak. Ogachi showed different MS cloud growth features in the first (existing fracture dominant) and second (stress consistent) stimulations. Another EGS field, Pohang (Korea), showed MS cloud extension behavior that was too difficult to interpret.

Other EGS fields including Cooper Basin, Australia, and Fenton Hill, United States, exhibit findings opposite to those noted in our study. In both fields, the MS clouds extended to the direction not related to *in-situ* stress. These phenomena was attributed to the strong preference for existing fracture distributions. In Cooper Basin, there were almost all subhorizontal sets of existing fractures that led to a very thin MS cloud (Baisch et al., 2006), which is difficult to attribute to *in-situ* stress information. In Fenton Hill, the dominant existing fracture sets were not consistent with the current *in-situ* stress state that led to MS cloud extension off the maximum horizontal stress direction (Norbeck et al., 2018); however, the MS cloud shape ratio was consistent with the stress ratio.

Thus, we conclude that if there are sufficient variations in existing fractures in the fields, the MS cloud growth process is controlled by *in-situ* stress, and the MS cloud shape can be predicted by the *in-situ* stress ratio. However, in fields with strong existing fracture preferences with few variations, the distribution of existing fractures is likely to have a dominant role in determining the MS cloud shape. It is very challenging to predict the shape of the MS cloud in these cases. The existing fracture distribution information from borehole logging would be a key to determining the dominant parameter for MS cloud geometry, as well as the numerical modeling approach (Norbeck et al., 2018).

Table 1. Summary of MS cloud growth behavior and consistency with *in-situ* stress for EGS/HDF fields

Field	Num. of MS event	Natural fracture	Stress regime	S_{Hmax} orientation	MS cloud orientation	Stress ratio	MS cloud dimension	Consistency with *in-situ* stress	Reference
Soultz-sous-Forêts, France, 1993	10,000 (located)	N-S vertical/ Stress consistent	SS or NF	N170°E ± 15°	N25°W	1:1:0.5	1: 0.8: 0.3	Stress consistent	(Baria et al., 1999; Evans, 2005; H Moriya et al., 2003; Hirokazo Moriya et al., 2002)
Cooper Basin, Australia, 2003	11,000 (located)	Subhorizontal	RF	N110°E	NNE-SSW	NA	1: 0.75: 0.1	Existing fracture dominant	Baisch et al., 2006; Reynolds et al., 2005
Fenton hill, US, 1983		N30°W	SS or NF	N30°E	NNW-SSE	1:1:0.5	1:1:0.2	Existing fracture dominant	Brown, 2012; Norbeck et al., 2018
Desert Peak, US, 2010, 2011	303 (located) 2200 (triggered)	Normal fault: ESE and WNW	SS or NF	N24°E	NNE-SSW	1:1~0.8: 0.6	1: 1: 0.2	Stress consistent	Zemach et al., 2017 Lutz et al., 2009 Davatzes & Hickman, 2009
Pohang, South Korea, 2017	519 (located)	NA	RF	N77°E	N214°E	1:0.5:0.4	1:0.5:0.2	Stress inconsistent	Korean Government Commission, 2019; Ellsworth et al., 2019
Helsinki, Finland, 2018	6150 (located)	NW-SE	SS	N110°E	NW-SE	1:0.75:0.45	NA	Stress consistent	Kwiatek et al., 2019

Hijiori, Japan, 1986	~200 (located)	Various/stress consistent	NF	EW	strike in the E-W, dipping in N	1:0.7:0.6	1:1:0.4	Stress consistent	Sasaki & Kaieda, 2002; Tezuka & Niitsuma, 2000; Oikawa and Yamaguchi, 2000
Ogachi, Japan, 1992	1554 (1st)	NE-SW or NNE-SSW/ High dip	SS or NF	EW	N20°E (1st)	1:1:0.9	1:0.5:0.2 (1st)	Existing fracture dominant (1st)	Kaieda et al., 1992 Hori et al., 1994 Kaieda et al., 2010
	1000 (2nd) (located)	Highly developed in shallow part (1st)	SS or NF	EW	N100°E (2nd)	1:0.6:0.5	1:0.5:0.25 (2nd)	Stress consistent (2nd)	

SS indicates strike-slip type, NF indicates normal fault type, and RF indicates reverse fault type

5 Conclusions

This study investigated how microseismic cloud grows during hydraulic stimulation by applying PCA to a time series of microseismic hypocenter distribution observed at the Basel EGS hydraulic stimulation project. Through PCA, the orientation of MS cloud growth was derived quantitatively and macroscopically. The MS cloud behavior characterized by PCA was compared with *in-situ* stress information, and their correlation was discussed and compared with those observed for other field cases.

The main conclusions of this study are:

- The MS cloud growth did not always extend to the maximum principal stress direction but did extend in the plane perpendicular to the minimum principal stress direction by the influence of the intermediate principal stress.
- The MS cloud shape ratios estimated using PCA results in 2D (horizontal or cross-sectional), and 3D were scaled with *in-situ* (effective) stress ratios. The MS cloud from different depth sections showed a close aspect ratio to the effective horizontal stress ratio, although the extension of the cloud in the direction of the least principal stress was overestimated. The cross-sectional MS cloud along the orientation of S_{Hmax} was circular, reflecting the very close stress magnitude of S_{Hmax} and S_v.
- The apparent permeability tensor estimated from microseismic hypocenter distribution data showed a good agreement with MS cloud growth in terms of orientation and magnitude relation. The MS cloud shape can be attributed to this permeability anisotropy, which should be a function of *in-situ* stress.
- Insights from this study are applicable to the MS cloud growth features for different EGS/HDR fields, especially when existing fractures show large variations (stress consistent case). However, there are other cases where the strong preference for existing fracture may play a more dominant role in controlling MS cloud growth.

In this study, we heuristically determined that MS cloud growth direction and shape are mainly controlled by *in-situ* stress, particularly where existing fractures show great variability, such as in the case of Basel. This study advances the understanding of the reservoir creation process, especially in a macroscopic sense. Further knowledge gaps need to be addressed for a more complete understanding of the reservoir creation process, including the physical explanation of how MS cloud shape or apparent permeability can be related to the stress ratio. In future research, systematic evaluation between the MS cloud shape and *in-situ* stress on various existing fracture distribution conditions should be carried out with numerical simulation. Finally, the findings of this study also emphasize the importance of reliable stress measurements to provide more meaningful information on the reservoir creation process.

Acknowledgments, Samples, and Data

The authors declare no conflicts of interest. We thank N. Watanabe for discussions and comments on the manuscript. This study was supported by an R&D project for super-critical geothermal field development supported by NEDO. Part of the work was carried out under the Collaborative Research Project of the Institute of Fluid Science, Tohoku University. Any use of trade, firm, or product names is for descriptive purposes only and does not imply endorsement by the U.S. Government.

Data Availability Statement

The microseismic catalog data containing the location, magnitude, and cluster information is uploaded to the MIT institutional repository.

References

Asanuma, H., Kumano, Y., Hotta, A., Niitsuma, H., Schanz, U., & Häring, M. (2007). Analysis of microseismic events from a stimulation at Basel, Switzerland. *GRC Transactions*, *31*, 265–270.

Asanuma, H., Kumano, Y., Niitsuma, H., Schanz, U., & Häring, M. (2008). Interpretation of reservoir structure from super-resolution mapping of microseismic multiplets from stimulation at Basel, Switzerland in 2006. *GRC Transactions, 32*, 65-70.

Baisch, S., Weidler, R., Vörös, R., Wyborn, D., & de Graaf, L. (2006). Induced seismicity during the stimulation of a geothermal HFR reservoir in the Cooper Basin, Australia. *Bulletin of the Seismological Society of America*, *96*(6), 2242–2256. https://doi.org/10.1785/0120050255

Baria, R., Baumgärtner, J., Gérard, A., Jung, R., & Garnish, J. (1999). European HDR research programme at Soultz-sous-Forets (France) 1987-1996. *Geothermics*, *28*(4–5), 655–669. https://doi.org/10.1016/S0375-6505(99)00036-X

Barton, C. A., Zoback, M. D., & Moos, D. (1995). Fluid flow along potencially active faults in crystalline rock. *Geology*, *23*(8), 683–686. https://doi.org/10.1130/0091-7613(1995)023<0683

Brown , D., Duchane, D., Heiken, G., & Hriscu, V. (2012). Mining the Earth's Heat: Hot Dry Rock Geothermal Energy. Springer.

Charléty, J., Cuenot, N., Dorbath, L., Dorbath, C., Haessler, H., & Frogneux, M. (2007). Large earthquakes during hydraulic stimulations at the geothermal site of Soultz-sous-Forêts. *International Journal of Rock Mechanics and Mining Sciences*, *44*(8), 1091–1105. https://doi.org/10.1016/j.ijrmms.2007.06.003

Davatzes, N., & Hickman, H. (2009). Fracture, Stress and Fluid Flow Prior to Stimulation of Well 27-15, Desert Peak, Nevada, EGS project, Proceedings of the 34th Workshop on Geothermal Reservoir Engineering, Stanford, CA.

Deichmann, N., & Giardini, D. (2009). Earthquakes induced by the stimulation of an enhanced geothermal system below Basel (Switzerland). *Seismological Research Letters*, *80*(5), 784–798. https://doi.org/10.1785/gssrl.80.5.784

Deng, A., & Stauffer, D. R. (2006), On improving 4-km mesoscale model simulations. *Journal of Applied Meteorology and Climatology*, *45*(3), 361–381. https://doi.org/10.1175/JAM2341.1

Dyer, B. C., Schanz, U., Ladner, F., Häring, M. O., & Spillman, T. (2008). Microseismic imaging of a geothermal reservoir stimulation. *The Leading Edge*, *27*(7), 856. https://doi.org/10.1190/1.2954024

Dyer, B. C., Schanz, U., Spillmann, T., Ladner, F., & Häring, M. O. (2010). Application of microseismic multiplet analysis to the Basel geothermal reservoir stimulation events. *Geophysical Prospecting*, *58*(5), 791–807. https://doi.org/10.1111/j.1365-2478.2010.00902.x

Ellsworth, W. L. (2013). Injection-induced earthquakes. *Science*, *341*(6142), 1225942. https://doi.org/10.1126/science.1225942

Ellsworth, W. L., Giardini, D., Townend, J., Ge, S., & Shimamoto, T. (2019). Triggering of the Pohang, Korea, Earthquake (Mw 5.5) by enhanced geothermal system stimulation. *Seismological Research Letters*, *90*(5), 1844–1858. https://doi.org/10.1785/0220190102

Evans, K. F. (2005). Permeability creation and damage due to massive fluid injections into granite at 3.5 km at Soultz: 2. Critical stress and fracture strength. *Journal of Geophysical Research B: Solid Earth*, *110*(4), 1–14. https://doi.org/10.1029/2004JB003169

Evans, K. F., Moriya, H., Niitsuma, H., Jones, R. H., Phillips, W. S., Genter, A., et al. (2005). Microseismicity and permeability enhancement of hydrogeologic structures during massive fluid injections into granite at 3 km depth at the Soultz HDR site. *Geophysical Journal International*, *160*(1), 388–412. https://doi.org/10.1111/j.1365-246X.2004.02474.x

Evans, K. F., Zappone, A., Kraft, T., Deichmann, N., & Moia, F. (2012). A survey of the induced seismic responses to fluid injection in geothermal and CO_2 reservoirs in Europe. *Geothermics*, *41*, 30–54. https://doi.org/10.1016/j.geothermics.2011.08.002

Gharti, H. N., Oye, V., Roth, M., & Kuhn, D. (2010). Automated microearthquake location using envelope stacking and robust global optimization. *Geophysics*, *75*(4). https://doi.org/10.1190/1.3432784

Grigoli, F., Cesca, S., Krieger, L., Kriegerowski, M., Gammaldi, S., Horalek, J., et al. (2016). Automated microseismic event location using Master-Event Waveform Stacking. *Scientific Reports*, *6*, 25744. https://doi.org/10.1038/srep25744

Häring, M. O., Schanz, U., Ladner, F., & Dyer, B. C. (2008). Characterisation of the Basel 1 enhanced geothermal system. *Geothermics*, *37*(5), 469–495. https://doi.org/10.1016/j.geothermics.2008.06.002

Herrmann, M., Kraft, T., Tormann, T., Scarabello, L., & Wiemer, S. (2019). A consistent high-resolution catalog of induced seismicity in Basel based on matched filter detection and tailored post-processing. *Journal of Geophysical Research: Solid Earth*, *124*(8), 8449–8477. https://doi.org/10.1029/2019JB017468

Hill, D. P. (1977). A model for earthquake swarms. *Journal of Geophysical Research*, *82*(8), 1347. https://doi.org/10.1029/JB082i008p01347

Hori, Y., Kitano, K., & Kaieda. (1994). Outline of Ogachi project for HDR geothermal power in Japan, *GRC Transactions*, 18, 439–443

Hubbert, M. K., & Willis, D. G. (1972). Mechanics of hydraulic fracturing. *Transactions of Society of Petroleum Engineers of AIME*, *210*, 153–163.

https://doi.org/https://doi.org/10.2118/686-g

Ito, T., & Zoback, M. D. (2000). Fracture permeability and in situ stress to 7 km depth in the KTB Scientific Drillhole. *Geophysical Research Letters*, *27*(7), 1045–1048.

Kaieda, H. Ito, H., Kiho, K., Suzuki, K., Suenaga, H., & Shin, K. (1992). Ogachi project for HDR geothermal power in Japan first hydraulic fracturing results, *GRC Transactions*, *16*, 493–496.

Kaieda, H., Sasaki, S., & Wyborn, D. (2010). Comparison of Characteristics of Microearthquakes Observed during Hydraulic Stimulation Operations in Ogachi, Hijiori and Cooper Basin HDR Projects, *Proceedings of the World Geothermal Congress*.

Kraft, T., & Deichmann, N. (2014). High-precision relocation and focal mechanism of the injection-induced seismicity at the Basel EGS. *Geothermics*, *52*, 59–73. https://doi.org/10.1016/j.geothermics.2014.05.014

Korean Government Commission. (2019). Summary Report of the Korean Government Commission on Relations between the 2017 Pohang Earthquake and EGS Project, *Geological Society of Korea*, Seoul, South Korea, doi: 10.22719/KETEP-20183010111860.

Kwiatek, G., Saarno, T., Ader, T., Bluemle, F., Bohnhoff, M., Chendorain, M., et al. (2019). Controlling fluid-induced seismicity during a 6.1-km-deep geothermal stimulation in Finland. *Science Advances*, *5*(5), 1–12. https://doi.org/10.1126/sciadv.aav7224

Lutz, S. J., Hickman, S., Davatzes, N., Zemach, E.,Drakos, P., & Robertson-Tait, A. (2010). Rock Mechanical Testing and Petrologic Analysis in Support of Well Stimulation Activities at the Desert Peak Geothermal Field, Nevada. *Proceedings of the 35th Workshop on Geothermal Reservoir Engineering*, Stanford, CA.

Majer, E. L., Baria, R., Stark, M., Oates, S., Bommer, J., Smith, B., & Asanuma, H. (2007). Induced seismicity associated with enhanced geothermal systems. *Geothermics*, *36*(3), 185–222. https://doi.org/10.1016/j.geothermics.2007.03.003

Miller, S. A. (2015). Modeling enhanced geothermal systems and the essential nature of large-scale changes in permeability at the onset of slip. *Geofluids*, *15*(1–2), 338–349. https://doi.org/10.1111/gfl.12108

Moriya, H, Niitsuma, H., & Baria, R. (2003). Multiplet-clustering analysis reveals structural details within the seismic. *Bulletin of the Seismological Society of America*, *93*(4), 1606–1620. https://doi.org/10.1785/0120020072

Moriya, Hirokazo, Nakazato, K., Niitsuma, H., & Baria, R. (2002). Detailed fracture system of the Soultz-sous-Forêts HDR field evaluated using microseismic multiplet analysis. *Pure and Applied Geophysics*, *159*(1–3), 517–541. https://doi.org/10.1007/PL00001263

Mukuhira, Y., Dinske, C., Asanuma, H., Ito, T., & Häring, M. O. (2017). Pore pressure behavior at the shut-in phase and causality of large induced seismicity at Basel, Switzerland. *Journal of Geophysical Research: Solid Earth*, *122*(1), 411–435. https://doi.org/10.1002/2016JB013338

Mukuhira, Y., Fuse, K., Naoi, M., Fehler, M. C., Moriya, H., Ito, T., et al. (2018). Hybrid focal mechanism determination: Constraining focal mechanisms of injection induced seismicity using in situ stress data. *Geophysical Journal International*, *215*(2), 1427–1441.

https://doi.org/10.1093/GJI/GGY333

Mukuhira, Yusuke, Asanuma, H., Niitsuma, H., & Häring, M. O. (2013). Characteristics of large-magnitude microseismic events recorded during and after stimulation of a geothermal reservoir at Basel, Switzerland. *Geothermics*, *45*, 1–17. https://doi.org/10.1016/j.geothermics.2012.07.005

Nasseri, M. H. B., Goodfellow, S. D., Lombos, L., & Young, R. P. (2014). 3-D transport and acoustic properties of Fontainebleau sandstone during true-triaxial deformation experiments. *International Journal of Rock Mechanics and Mining Sciences*, *69*, 1–18. https://doi.org/10.1016/j.ijrmms.2014.02.014

Norbeck, J. H., McClure, M. W., & Horne, R. N. (2018). Field observations at the Fenton Hill enhanced geothermal system test site support mixed-mechanism stimulation. *Geothermics*, *74*(March), 135–149. https://doi.org/10.1016/j.geothermics.2018.03.003

Oikawa, Y. & Yamaguchi, T. (2000). Stress Measurement using Rock Core in an HDR Field, *Proceedings of the World Geothermal Congress*, 3819–3822.

Reynolds, S.D., Mildren, S.D., Hillis, R.R., Meyer, J.J., & Flottmann, T. (2005). Maximum horizontal stress orientations in the Cooper Basin, Australia: Implications for plate-scale tectonics and local stress sources. *Geophysical Journal International*, *160*, 331–343.

Pine, R. J., & Batchelor, A. S. (1984). Downward migration of shearing in jointed rock during hydraulic injections. *International Journal of Rock Mechanics and Mining Sciences And*, *21*(5), 249–263. https://doi.org/10.1016/0148-9062(84)92681-0

Rice, J. R. (1993). Spatio-temporal complexity of slip on a fault. *Journal of Geophysical Research*, *98*(B6), 9885–9907. https://doi.org/10.1029/93JB00191

Rice, J. R. (1992). Chapter 20 Fault stress states, pore pressure distributions, and the weakeness of the San Andreas fault. *International Geophysics*, 51, 475-503, San Diego, CA: Press. https://doi.org/10.1016/j.jvolgeores.2021.107317.

Roff, A., Phillips, W.S., & Brown, D.W. (1996). Joint structures determined by clustering microearthquakes using waveform amplitude ratios. *International Journal of Rock Mechanics and Mining Sciences & Geomechanics Abstracts*, *33*(6), 627-639.

Sasaki, S., & Kaieda, H. (2002). Determination of stress state from focal mechanisms of microseismic events induced during hydraulic injection at the Hijiori hot dry rock site. *Pure and Applied Geophysics*, *159*(1), 489–516. https://doi.org/10.1007/PL00001262

Shapiro, S. A., Huenges, E., & Borm, G. (1997). Estimating the crust permeability from fluid-injection-induced seismic emission at the KTB site. *Geophysical Journal International*, *131*(2), 5–8. https://doi.org/10.1111/j.1365-246X.1997.tb01215.x

Shapiro, S. A., Audigane, P., & Royer, J. J. (1999). Large-scale in situ permeability tensor of rocks from induced microseismicity. *Geophysical Journal International*, *137*(1), 207–213. https://doi.org/10.1046/j.1365-246X.1999.00781.x

Shu, L., McIsaac, K., & Osinski, G. R. (2018). Learning spatial-spectral features for hyperspectral image classification. *IEEE Transactions on Geoscience and Remote Sensing*, *56*(9), 5138–5147. https://doi.org/10.1109/TGRS.2018.2809912

Sibson, R. H. (1996). Structural permeability of fluid-driven fault-fracture meshes. *Journal of Structural Geology*, *18*(8), 1031–1042. https://doi.org/10.1016/0191-8141(96)00032-6

Soma, N., Niitsuma, H., & Baria, R. (2007). Reflection imaging of deep reservoir structure based on three-dimensional hodogram analysis of multicomponent microseismic waveforms. *Journal of Geophysical Research: Solid Earth*, *112*(11), 1–14. https://doi.org/10.1029/2005JB004216

Tezuka, K., & Niitsuma, H. (2000). Stress estimated using microseismic clusters and its relationship to the fracture system of the Hijiori hot dry rock reservoir. *Developments in Geotechnical Engineering*, *84*(C), 55–70. https://doi.org/10.1016/S0165-1250(00)80007-3

Valley, B., & Evans, K. F. (2009). Stress orientation to 5 km depth in the basement below Basel (Switzerland) from borehole failure analysis. *Swiss Journal of Geosciences*, *102*(3), 467–480. https://doi.org/10.1007/s00015-009-1335-z

Valley, B., & Evans, K. F. (2015). Estimation of the stress magnitudes in Basel enhanced geothermal system. *Proceedings World Geothermal Congress 2015*.

Valley, B., & Evans, K. F. (2019). Stress magnitudes in the Basel enhanced geothermal system. *International Journal of Rock Mechanics and Mining Sciences*, *118*(November 2018), 1–20. https://doi.org/10.1016/j.ijrmms.2019.03.008

Vidale, J. E., & Shearer, P. M. (2006). A survey of 71 earthquake bursts across southern California: Exploring the role of pore fluid pressure fluctuations and aseismic slip as drivers. *Journal of Geophysical Research: Solid Earth*, *111*(5), 1–12. https://doi.org/10.1029/2005JB004034

Waldhauser, F., & Ellsworth, W. L. (2000). A double-difference earthquake location algorithm: Method and application to the Northern Hayward Fault, California. *Bulletin of the Seismological Society of America*, *90*(6), 1353–1368. https://doi.org/10.1785/0120000006

Watanabe, N., Hirano, N., & Tsuchiya, N. (2008). Determination of aperture structure and fluid flow in a rock fracture by high-resolution numerical modeling on the basis of a flow-through experiment under confining pressure. *Water Resources Research*, *44*(6), 1–11. https://doi.org/10.1029/2006WR005411

Willis-Richards, J., Watanabe, K., & Takahashi, H. (1996). Progress toward a stochastic rock mechanics model of engineered geothermal systems. *Journal of Geophysical Research*, *101*, 17481–17496.

Xue, L., Bürgmann, R., Shelly, D. R., Johnson, C. W., & Taira, T. (2018). Kinematics of the 2015 San Ramon, California earthquake swarm: Implications for fault zone structure and driving mechanisms. *Earth and Planetary Science Letters*, *489*, 135–144. https://doi.org/10.1016/j.epsl.2018.02.018

Yeo, I. W., De Freitas, M. H., & Zimmerman, R. W. (1998). Effect of shear displacement on the aperture and permeability of a rock fracture. *International Journal of Rock Mechanics and Mining Sciences*, *35*(8), 1051–1070. https://doi.org/10.1016/S0148-9062(98)00165-X

Zemach, E., Drakos, P., Spielman, P., & Akerley, J. (2013). *Desert Peak Enhanced Geothermal Systems (EGS) Project (Draft Final Report)*, doi:10.2172/1373310.

Ziegler, M., & Evans, K. F. (2020). Comparative study of Basel EGS reservoir faults inferred from analysis of microseismic cluster datasets with fracture zones obtained from well log analysis. *Journal of Structural Geology*, *130*(October 2019), 103923. https://doi.org/10.1016/j.jsg.2019.103923

Ziegler, M., Valley, B., & Evans, K. F. (2015). Characterization of natural fractures and fracture sones of the Basel EGS reservoir inferred from geophysical logging of the Basel-1 well. *Proceedings World Geothermal Congress 2015*.

Zoback, M. (2007). *Reservoir Geomechanics*, Cambridge University Press.

Appendix

Suppose M is the 3 by *n* matrix consisted by earthquake locations in consideration.

$$\mathbf{M} = \begin{pmatrix} x_1 & \cdots & x_n \\ y_1 & \cdots & y_n \\ z_1 & \cdots & z_n \end{pmatrix} \tag{A1}$$

Based on **M**, we get correlation matrix **C** and then premultiply and postmultiply **D** to get the variance covariance matrix $\boldsymbol{\Sigma}$.

$$\boldsymbol{\Sigma} = \mathbf{DCD} \tag{A2}$$

where, $\mathbf{D} = \begin{pmatrix} \sigma_x & 0 & 0 \\ 0 & \sigma_y & 0 \\ 0 & 0 & \sigma_z \end{pmatrix}$ (A3).

Here, σ_n (n=x, y, z) is the standard deviation on each basis.

Eigenvalue decomposition is performed on $\boldsymbol{\Sigma}$ to get the eigen values $\boldsymbol{\Lambda}$ and corresponding eigen vectors V, which are principal components and their vectors.

$$\boldsymbol{\Sigma} = V\boldsymbol{\Lambda}V^T \tag{4}$$

where $\boldsymbol{\Lambda} = diag[\lambda_1, \lambda_2, \lambda_3]$, $V = [v_1, v_2, v_3]$.